Materials Today Bio 25 (2024) 100949

Contents lists available at ScienceDirect

Materials Today Bio

journal homepage: www.journals.elsevier.com/materials-today-bio

Rapid innervation and physiological epidermal regeneration by bioengineered dermis implanted in mouse

Claudia Mazio [a,1], Isabella Mavaro [b,a,1], Antonio Palladino [c], Costantino Casale [d], Francesco Urciuolo [e], Andrea Banfi [f], Livia D'Angelo [b], Paolo A. Netti [a,d,e], Paolo de Girolamo [b], Giorgia Imparato [a,*], Chiara Attanasio [b]

[a] Istituto Italiano di Tecnologia, Center for Advanced Biomaterials for HealthCare@CRIB, Italy
[b] University of Naples Federico II, Department of Veterinary Medicine and Animal Production, Italy
[c] University of Naples Federico II, Department of Agricultural Sciences, Italy
[d] University of Naples Federico II, Interdisciplinary Research Centre on Biomaterials (CRIB), Italy
[e] University of Naples Federico II, Department of Chemical, Materials and Industrial Production Engineering, Italy
[f] Basel University Hospital and University of Basel, Department of Biomedicine, Switzerland

ARTICLE INFO

Keywords:
Human dermis equivalent
Endogenous ECM
In vivo skin defect model
Innervation
Vascularization
Epidermal appendages

ABSTRACT

Tissue-engineered skin substitutes are promising tools to cover large and deep skin defects. However, the lack of a synergic and fast regeneration of the vascular network, nerves, and skin appendages limits complete skin healing and impairs functional recovery. It has been highlighted that an ideal skin substitute should mimic the structure of the native tissue to enhance clinical effectiveness. Here, we produced a pre-vascularized dermis (PVD) comprised of fibroblasts embedded in their own extracellular matrix (ECM) and a capillary-like network. Upon implantation in a mouse full-thickness skin defect model, we observed a very early innervation of the graft in 2 weeks. In addition, mouse capillaries and complete epithelialization were detectable as early as 1 week after implantation and, skin appendages developed in 2 weeks. These anatomical features underlie the interaction with the skin nerves, thus providing a further cue for reinnervation guidance. Further, the graft displays mechanical properties, collagen density, and assembly features very similar to the host tissue. Taken together our data show that the pre-existing ECM components of the PVD, physiologically organized and assembled similarly to the native tissue, support a rapid regeneration of dermal tissue. Therefore, our results suggest a promising potential for PVD in skin regeneration.

1. Introduction

Tissue engineering aims to fabricate organ and tissue equivalents under controlled conditions, to allow their transplantation into patients with reduced capacity to regenerate or repair their own tissues and organs. Skin is the largest "organ" of the body with the main function of protecting internal organs from the surrounding environment, therefore, it is continuously exposed to the risk of damage [1]. Over the last several years, many efforts have been made by the scientific community to develop advanced strategies to efficiently engineer and produce skin substitutes [2–5]. These latter, made of biomaterials, cells, and bioactive agents, hold the potential to accelerate wound recovery by stimulating cell migration and hastening vascularization and epithelialization [6–10]. The engineered tissue should be made up of all the layers of the skin including appendages and guarantee the development of functional nervous and vascular networks. All these features lead to the integration of the construct with the surrounding host tissue without scar formation [11]. After the initial success obtained with the manufacture of epithelium substitutes, many efforts were focused on creating the dermal component of the skin [12]. The development of human dermal substitutes is, indeed, essential to achieve a proper integration of the graft and successful wound healing, especially when deep and large critically sized defects have to be managed [13]. Human dermal substitutes can be implanted alone or in combination with split-thickness skin grafts (STSG) to overcome the risk of contracture, poor cosmetic outcome, physical disability, and reduced pliability of single STSG

* Corresponding author.
E-mail address: giorgia.imparato@iit.it (G. Imparato).
[1] These two authors contributed equally to this research.

https://doi.org/10.1016/j.mtbio.2024.100949
Received 25 September 2023; Received in revised form 2 January 2024; Accepted 6 January 2024
Available online 10 January 2024

transplantation. Natural/synthetic polymers [14], have been used to fabricate hydrogels [7,15] and nano/micro-fibers [16], while nano/micro-particles, foams [16], and sponges [17] have been used as tissue scaffolds. These latter constructs have been combined with cells and cultured to generate functional tissues targeted to cover the damaged wound site but also to accelerate and optimize the healing process by interacting with the surrounding tissue [18]. However, there are still open challenges associated with skin graft use that limit their translation into the clinic, i.e. the need to mimic the organization and the coordinated interplay of the multiple cell types, promote the integration between the constructs and the host vasculature and nervous system, as well as to support the development of functional skin appendages [19]. Ensuring sustained engraftment and long-term survival of a transplanted skin analog strongly relies on the timely development of capillaries and large blood vessels to support early vascularization. Indeed, although graft vascularization could take place via growth and invasion of the implanted tissue by the patient's own blood vessels, this process is usually slow, leaving cells without oxygen and nutrients for too long [20]. In this condition, cell survival and proliferation are strongly inhibited, and, in turn, efficient wound repair is difficult to obtain. Moreover, since nerve regeneration is highly dependent on newly formed blood vessels, nerve regeneration is almost completely inhibited when blood supply is absent [11,21]. In this perspective, tissue pre-vascularization, obtained by introducing vascular cells that form vessel-like structures and mature capillary networks in vitro before implantation, seems to be a promising strategy to boost the vascularization of skin constructs and, in turn, to sustain their innervation [22]. Some successful attempts reported in the literature include the model proposed by Chen et al. [23] who produced pre-vascularized sheets composed of human mesenchymal cells (PHCS) and subsequently implanted them in a rat full-thickness skin wound model coupled with an autologous STSG. This study demonstrated that PHCS implantation induced high neovascularization in the early stages and established a robust blood micro-circulation to support graft survival and tissue regeneration. Moreover, the authors demonstrated that PHCS implantation significantly reduced skin contraction, improved cosmetic appearance, and preserved the largest amount of skin appendages compared to the STSG control group, although they did not investigate the presence of neural structures. The major advantage of PHCS was the retrieval of the intact cell layers along with their naturally organized extracellular matrix (ECM). This aspect contributed to accelerating the regeneration of dermal tissue through the mitigation of the cellular processes associated with graft fibrosis and contraction [23]. In this scenario, we recently highlighted the pivotal role of endogenous ECM, which includes all the main components of the native dermis (i.e. collagen, elastin, proteoglycans, fibronectin), in guiding capillary-like structure formation in vitro and in sustaining fast and functional vascularization when the same tissue was subcutaneously implanted in mouse [13]. Although the model was very effective in evaluating the formation of the functional anastomosis with the host vasculature, progress toward clinical translation would require implantation of the pre-vascularized dermis in a more physiological model resembling the usual procedure for skin replacement. Therefore, here we replaced a portion of mouse skin with the pre-vascularized dermis in a full-thickness skin defect model, showing that a physiological environment allows tissue re-epithelialization, vascularization, preservation of skin appendages, and very early re-innervation. The latter, indeed, has never been observed before 8 weeks after implantation and still represents an open challenge to improve the quality of skin analogs [11,24–26]. In contrast, here we found that, in the presence of pre-vascularized ECM with a physiological dermal ECM architecture, re-innervation occurs already 2 weeks after implantation.

2. Materials and methods

2.1. Pre-vascularized human dermis equivalent fabrication

2.1.1. Cell culture

Human fibroblasts were extracted and cultured as previously described [13]. Human dermal fibroblasts (HDFs) were cultured in minimum essential medium (MEM) supplemented with 20% of fetal bovine serum (FBS), 2% of Non- Essential Aminoacids, 1% of L-Glutamine, and 1% of penicillin/streptomycin, until passage 8. Human umbilical vein endothelial cells (HUVECs from GIBCO) were cultured in supplemented VascuLife® until P4. The final concentrations of the components in the complete kit composed of the basal medium along with associated supplements and growth factors were: Fibroblast growth factor (FGF) 5 ng/ml, Ascorbic acid 50 μg/ml, hydrocortisone hemisuccinate 1 μg/ml, FBS 2%, L Glutamine 10 mM, insulin-like growth factor (IGF-1) 105 ng/ml, epidermal growth factor (EGF) 5 ng/ml, vascular endothelial growth factor (VEGF) 5 ng/ml, Heparin sulfate 0.75U/ml, gentamicin 30 mg/ml and amphotericin 15 μg/ml. Cells were maintained at 37 °C in a humidified atmosphere containing 5% CO2 in the incubator.

2.1.2. Micro-scaffold production

Gelatin porous micro-scaffolds were prepared according to a modified double emulsion oil/water/oil (O/W/O) protocol. And stabilized by crosslinking reaction with 4% w/w glyceraldehyde [27].

2.1.3. Human dermal micro-tissue production

About 11 HDFs at P8 were seeded for micro-scaffold, as previously described [13]. Cells were cultured into spinner flask bioreactors (Integra) in continuous agitation (30 rpm) until the formation of micro-tissue units composed of micro-scaffolds and HDFs embedded into their own extracellular matrix (ECM). The culture medium was the MEM supplemented with 20% FBS, 2% Non- Essential Aminoacids, 1% L-Glutamine, 1% penicillin/streptomycin, and 0.5 mM Ascorbic Acid (2-*O*-α-D-Glucopyranosiyl-LAscorbic- Acid TCI). The micro-tissue units were cultured for 9 days [13,28].

2.1.4. Pre-vascularized dermis equivalent production

After the 9 days culture, the micro-tissue units were assembled in a maturation chamber, designed *ad hoc* to obtain parallelepiped-shaped dermis macro-tissues, namely human dermis equivalent (HDE) (7 mm × 4 mm × 1 mm). The maturation chamber was placed on the bottom of a spinner flask bioreactor (Bellco biotechnology) and surrounded by MEM culture medium supplemented with 20% FBS, 2% Non- Essential Aminoacids, 1% L-Glutamine, 1% penicillin/streptomycin, and 0.5 mM Ascorbic Acid. The spinner was run at 60 rpm. After 5 weeks of culture, the assembling chamber was opened, and the dermis equivalent was collected. Endothelial cells, HUVECs at P4, were seeded as a drop on the surface of the samples, at a high density of about 10.000/15.000 cells for mm^2. Although the HUVECs are not derived from the dermis, we chose them since their use is very well documented for tissue engineering application due to their capacity to develop capillary-like structures when co-cultured with dermal fibroblasts [13,29–31]. HUVEC seeding was performed into low attach multiwells. Cells were suspended in 15 μl of the medium in order to avoid drop falling. After the seeding, samples were left at 37 °C for 2 h enabling endothelial cells adhesion. Afterwards, Vasculife medium was added up to completely cover the sample. From the day after the seeding, a medium composed of MEM and Vasculife was added in a 2:1 ratio. The culture medium was changed twice a week and samples were harvested after 10 days before implantation.

2.1.5. Characterization of the PVD: SHG imaging and multiphoton confocal microscopy

The pre-vascularized dermis (PVD) developed in vitro was characterized by multiphoton and confocal microscopy (TCS SP5 MP Leica) to

evaluate the presence of capillaries in the collagen matrix before implantation. Capillary-like structures were marked using the lectin Rho-UEAI (Rhodamine-Ulex europaeus I) whereas the matrix was observed through the second harmonic generation (SHG) signal of collagen fibers. The next paragraphs will describe the procedures followed for tissue implantation and explanted tissue characterization.

2.1.6. Implantation of PVD in a full-thickness skin defect model

Animal studies were performed following the guidelines of the European Communities Council directive (2010/63/EU). Immunodeficient nu/nu mice 6/7 weeks old (Harlan) (n = 20) were housed in single cages for 10 days before surgery. Baytril (2,5%; 25 mg/ml) antibiotic solution was subcutaneously administered to the animals on the day of surgery and for the following 6 days in drinking water (10 mg/kg). Mice received deep anaesthesia by intraperitoneal injection of ketamine (75 mg/kg body weight) and xylazine (15 mg/kg body weight). Intraoperative analgesia has been ensured by subcutaneous administration of Carprofen (4 mg/kg) immediately after anaesthesia. The surgical procedure began when the required anaesthesia level was obtained. After sanitization with 10% Iodopovidone (Betadine®) a 7 mm × 4 mm sheet of skin was cut and removed for construct implantation from the back of the mice, centrally and distally to the shoulder blades. Concerning the wound size, we considered a 0.28 cm^2 area (0.7 × 0.4 mm) according to the literature [32,33]. All mice were implanted with the pre-vascularized dermis. 3 M™ Tegaderm™ Transparent Film was positioned on the implantation area to preserve the graft by protecting it from any mechanical stress. Four animals were euthanized at different endpoints: 3, 7, 14, and 21 days after surgery. The retrieved tissues were fixed in formalin or paraformaldehyde for histological and immunofluorescence analysis, respectively. At day 21, immediately after retrieval, tissues were analyzed to assess their mechanical resistance via Indentation Test and then appropriately fixed.

2.1.7. Measure of the wound size

The wound size was calculated measuring the wound area on macroscopic picture with Image J. A ruler in the picture was used to set the scale bar in each picture. The wound area was manually traced with the freehand selection and analyzed by the "Measure" tool.

2.2. Characterization of the explanted tissue

2.2.1. Histology

Samples were fixed in Formalin 10% (Sigma) for 1 h at room temperature (RT) and washed in PBS1X. They were dehydrated in Ethanol from 75% to 100% and treated with Xylene (ROMIL) before paraffin embedding. Tissue slices 7 μm thick were cut by using a microtome (Thermo Scientific) and then deparaffinized with xylene. Sections were rinsed in ethanol from 100% to 75%, washed in water, and stained by Hematoxylin/Eosin (Bio Optica). The sections were mounted with Histomount Mounting Solution (Bio-Optica) and observed with a light microscope (Leica DMRA2). Tile scan images of the samples explanted at day 7, 14, and 21 after implant were performed with Leica LAS AF software.

2.2.2. Fluorescent staining on paraffin sections

Samples were fixed in formalin 10% (Sigma) for 1 h at RT and washed in PBS1X (Sigma), rinsed in Ethanol from 75% to 100% and treated with Xylene (ROMIL) before paraffin embedding. The day after tissue slices 7 μm thick were cut by using a microtome (Thermo Scientific) and then deparaffinized with xylene. Sections were rinsed in ethanol from 100% to 75% and washed in water, Triton 0,2%, and PBS1X. A heat-mediated unmasking with TRIS-EDTA (10 mM Tris Base, 1 mM Ethylenediamine tetra acetic acid Solution, 0.05% Tween 20, pH 9.0) for 30 min at 90 °C was carried on. Sections were washed in PBS1X, non-specific antigen binding was blocked using bovine serum albumin (BSA)1%, FBS 1%, MgCl2 0.5 Mm, and CaCl2 1 mM in PBS1X for 2 h at RT, then sections were incubated with Rho-UEA I (20 μg/ml) and 488-Griffonia Simplicifolia (200 μg/ml) over night (ON) at 4 °C in wet conditions. The morning after, samples were washed in PBS1X. Nuclei were stained with DAPI, and samples were observed by Confocal Leica TCS SP5 II. Immunofluorescence was performed to detect K75 (Keratin 75), CD133, BDNF (brain-derived neurotrophic factor), TrkB (Tropomyosin receptor kinase B), NGF (Nerve growth factor), TrkA (Tropomyosin receptor kinase A), and Prox-1 (Prospero homeobox 1) a heat-mediated citrate buffer (pH = 6, Thermo scientific) unmasking was performed, by completely covering the slices with the 1× solution (diluted in water)- Sections were then placed in a microwave until the temperature of the solution reached 95–100 °C. After 20 min of incubation, samples were left to cool at RT for about 1 h, washed with PBS, non-specific antigen binding was blocked with BSA1% and FBS 5% in PBS for 2 h at RT, then sections were incubated with the primary antibody ON at 4 °C in wet conditions. Primary antibodies were: K75, CD133, CD68, BDNF, TrkB, NGF, TrkA, Beta Tubulin III, and PROX-1. No unmasking was used for NF200 (Neurofilament 200) antibody. Samples were then washed in PBS and incubated with a secondary antibody (Alexa Fluor 546 1:500) for 1 h at RT. A detailed table of the primary antibodies is reported below (Table 1).

Table 1
List of the primary antibodies used in the study.

NAME	HOST SPECIES	PRODUCT CODE	COMPANY	DILUTION
K75	Rabbit	NBP1-87845	Novus Biological	1:50
CD133	Mouse	ab19898	Abcam	1:30
CD68	Mouse	ab955	Abcam	1:50
BDNF	Rabbit	ab108319	Abcam	1:100
TrkB	Rabbit	ab18987	Abcam	1:100
NGF	Rabbit	ab52918	Abcam	1:250
TrkA	Rabbit	sc-80398	Santa Cruz	1:50
NF200	Rabbit	N4142	Sigma-Aldrich	1:80
Beta-Tubulin	Rabbit	ab18207	Abcam	1:100
Vimentin (V9)	Mouse	11-9897-80 -	eBioscience™	1:500
PROX-1	Rabbit	P7124	Sigma	1:200

2.3. Quantitative image analysis for neutrophins and their receptors

Ten images per sample were acquired both at epithelium and dermis side of the implant and analyzed by ImageJ (ImageJ-win64 1.54f). In order to estimate the relative quantity of each protein per cell, the area corresponding to the fluorescent protein signal was thresholded, quantified (in μm^2), and the ratio protein/number of cells, obtained by counting cell nuclei stained by DAPI calculated with the "Analyze particles" tool of ImageJ tuning the particle size to perfectly fit the nuclear signals, imposing a minimum nuclear size of 50 μm^2.

2.4. Fluorescent staining of whole-mount samples

Samples were fixed in 4% Paraformaldehyde (Sigma Aldrich) for 30 min at RT, washed in PBS1X, permeabilized with 0,1% Triton (Sigma) in PBS1X for 5 min at RT, washed in PBS1X, and non-specific antigen binding was blocked in 1% BSA (Sigma) for 1 h at RT. Afterwards, samples were stained with Rhodamine Ulex Europaeus Agglutinin I (UEAI Vector Laboratories) at a final concentration of 20 μg/ml in blocking solution, and incubated at 4 °C in the dark, in order to mark the human endothelium. The morning after, samples were washed with PBS1X and the nuclei of all the cells were stained with Sytox Green (Invitrogen) for 20 min at RT.

2.5. Sample clarification

Stained samples were dehydrated by serial immersions, of 30 min

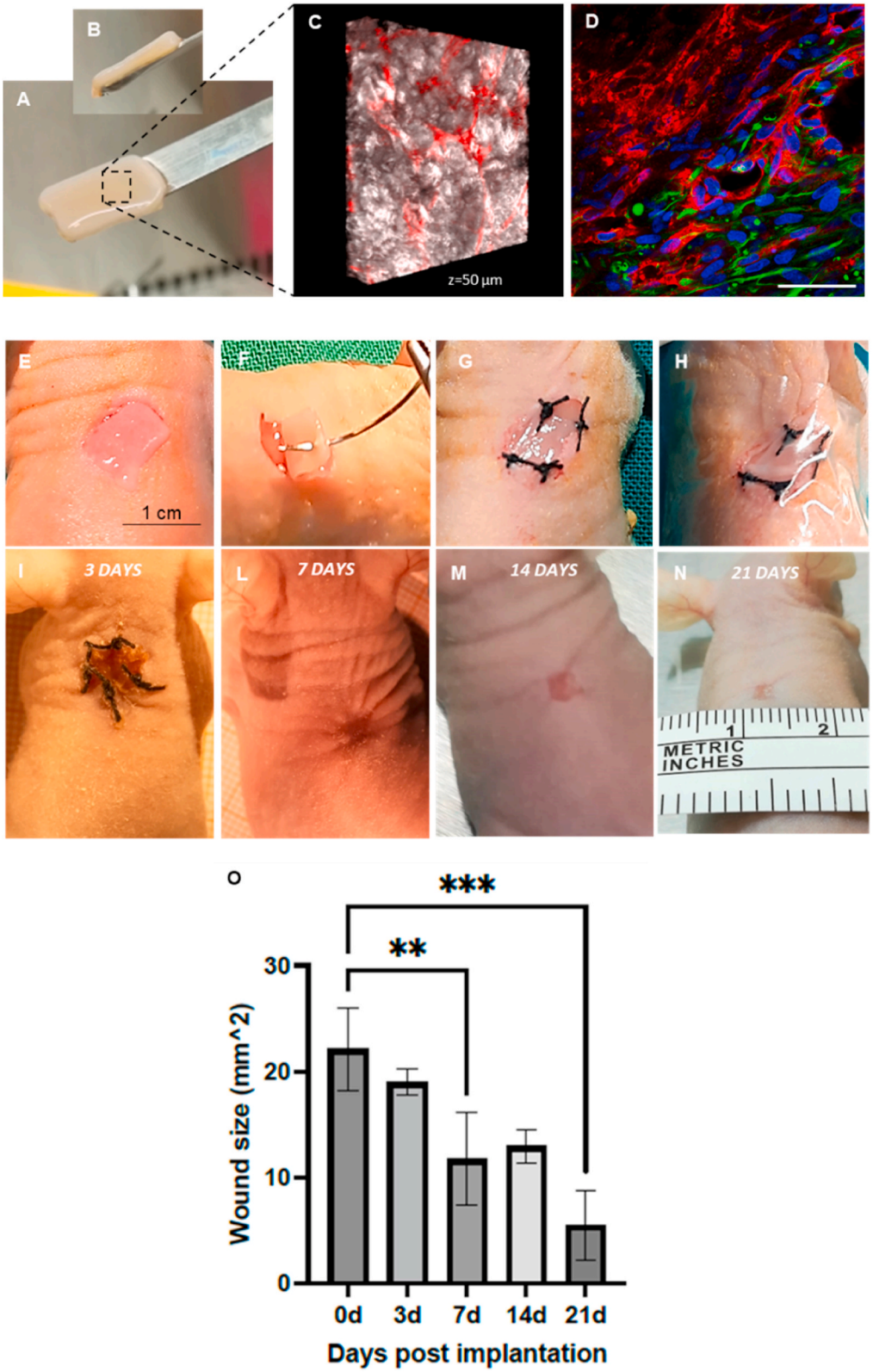

Fig. 1. Evolution of the implanted PVD. A-B Macroscopic image of PVD surface and lateral view, respectively. C. 3D view of the PVD via SHG and Rho-UEAI staining highlights collagen meshwork and vascularization potential. D. Confocal image of PVD highlights fibroblasts by vimentin immunolabeling (green) and capillary-like network by Rho-UEAI staining. Cell nuclei are counterstained with DAPI. Scale bar is 50 µm. E-H. Steps of the whole implantation procedure and suture. Graft integrity was ensured by 3 M™ Tegaderm™ Transparent Film. I–N. Timing of wound-healing process showing the well-integrated construct in the skin of all surged animals. The suture was necessary only the first week after surgery. O. Graphic of the wound size (mm^2) over time. Day 0 represents the size of the initial wound on the skin of the mouse; the reduction of the wound was observed 3, 7, 14 and 21 days after implantation. *p value < 0.05; **p value < 0.01.

each, in Methanol 50%, 70%, 80%, 90%, and 100%. A "BABB" solution was prepared with Benzyl Alcohol (BA) and Benzyl Benzoate (BB) (SIGMA) in a 1:2 ratio. Samples were moved into a glass bottle and treated with Methanol and "BABB" (1:1) for 4 h and then with "BABB" for 24 h at RT. Samples were observed into fluorodish by Confocal Leica TCS SP5 II. The procedure of sample staining and clarification was previously reported [13,34].

2.6. Multi-photon microscopy and second harmonic generation imaging

For Second Harmonic Generation (SHG) imaging, samples were fixed for 30 min with 4% paraformaldehyde and observed by a confocal microscope (TCS SP5 II Leica) combined with a Multiphoton microscope (Multiphoton Microscope stage Chamaleon Compact OPO-Vis, Coherent). Two-photon excited fluorescence was used to induce SHG and obtain high-resolution images of unstained collagen structures. The samples were observed by using λex = 840 nm (two photons) and λem = 415–425 nm. The SHG images were acquired with a resolution of 12 bit, 1024X1024 pixels by using a 25X water immersion objective (HCX IRAPO L 25.0X0.95 Water, n. a. 0.95).

2.7. Collagen amount quantification from SHG images

SHG images were analyzed by using ImageJ software to quantify the collagen fraction. To analyze the features of the collagenous ECM multiple regions of interest (ROI) in the stroma compartment were chosen by excluding the signal rising from the micro-scaffolds. The Collagen Fraction (%) was defined as the percentage of the ratio between bright pixels to total pixels in the selected ROI (Eq. (1)). The number of bright pixels was measured after thresholding to convert the pixels in the grey scale of the SHG image in black (255). The total number of pixels was the sum o the black (255) and white pixels in the selected ROI after black/white threshold.

$$\text{Collagen Fraction}(\%) = \frac{Nc}{Nb + Nc} * 100 \quad (1)$$

Nc and Nb represent the number of pixels from the collagenous and non-collagenous portion, respectively [35].

2.8. Collagen assembly degree from SHG images

SHG images were analyzed by ImageJ software. The degree of Collagen assembly (CAD) was evaluated by analyzing the Histogram of the SHG images to calculate the average intensity, as described by Eq. (2):

$$CAD = \frac{\sum_{i=0}^{255} Iipi}{\sum_{i=0}^{255} pi} \quad (2)$$

where I is the average intensity and Ii is the intensity corresponding to the pixel pi, which runs in the grey value interval from 0 to 255. The intensity I of collagen network is known to be proportional to the degree of assembly of the newly synthesized collagen [35].

2.9. Mechanical properties

The mechanical properties of the samples were analyzed, as previously described, by means of Piuma Nano-Indenter (Optics11), a displacement-controlled nano-indenter machine including a controller, an optical fiber, and a spherical probe [36]. The probe is attached to a spring cantilever connected to the end of an optical fiber that measures its deflection. Each sample was indented using a cantilever with a stiffness of 4.53 Nm^{-1}. The maximum indentation depth (h_{max}) was set at 10 μm for each indentation test that was performed in 5 different points of each sample. The tip radius (R_i) was 53.5 μm. During the test, the machine measured the load (F) and indentation (h) during the loading and the unloading phases. The calculation of the effective Young's modulus was obtained by fitting the part of the F-h curve below the 10% of F_{max} (maximum loading) with the Hertzian contact model [37] represented by the following equation (3):

$$F = (4/3)E_{eff}\sqrt{Ri} \bullet h^{3/2} \quad (3)$$

The analysis returns the effective (or reduced) Young's modulus (E_{eff}), in which the Poisson's ratio (ν) has not been considered (Supplementary Fig. S1). The "bulk" Young's modulus (E) is related to the effective or reduced Young's modulus (E_{eff}) by the following equation (4):

$$E = E_{eff}(1-\nu^2) \quad (4)$$

The Poisson's ratio has not been measured; therefore, we report as measure of the mechanical stiffness the effective (or reduced) Young's modulus (E_{eff}).

2.10. Statistical analysis

All the experiments have been performed in triplicate (N = 3). The graphics reports data as mean ± standard deviation (SD). For collagen fraction, collagen assembly degree and elastic modules, differences between groups were analyzed by ANOVA followed by Tukey HSD test. For the analysis of the wound area, data were analyzed by one-way ANOVA using multiple comparisons relative to t = 0. T for neutrophin and related receptor data were analyzed by *t*-Test with a 95% confidence level. P values < 0,05 (*), p values < 0.01 (**) and, p values < 0,001 (***) have been considered statistically significant.

3. Results and discussion

3.1. Pre-vascularized human dermis equivalent fabrication and implantation

The PVD was produced as previously reported [13]. According to the bottom-up bioengineering approach, the PVD (7 × 4 × 1 mm) (Fig. 1A and B) presented a capillary-like network embedded into a fibroblast-produced collagenous matrix (Fig. 1C) Here, to assess the main features of the PVD in vitro, we investigated collagen organization by SHG imaging (grey color), CLS morphology by Rho-UEAI, and fibroblast phenotype by vimentin immunolabeling (in green) (Fig. 1C and D). The latter is a widely recognized marker of fibroblasts that tunes signaling cascades regulating cell migration and ECM remodelling [38] As previously demonstrated, the physiological milieu of the 3D model guided the endothelial cells toward a functional in vitro vasculogenesis in a very short time (1 week). This feature was displayed by the homogeneously distributed capillary-like network developed by HUVEC in the PVD. In addition, previous results [13] showed that after 7 days of subcutaneous implantation in mice, the CLS of the PVD created functional anastomosis with the host vasculature in contrast to the non-pre-vascularized model (Supplementary Fig. S2). Here we used a more physiological approach to investigate the wound-healing process through the implantation of the PVD in a full-thickness skin defect model. A full-thickness skin defect 7 mm × 4 mm was made on the dorsal side of the mouse and replaced by the PVD by suturing it to the surrounding skin (Fig. 1E–H). In contrast to the subcutaneous implant used in our previous study [13], this "skin replacement model" is more effective to reveal the role of the PVD as a skin substitute after injury. The different evolution of the two kinds of graft after implantation is reported in Supplementary Fig. S3. The image displays a higher degree of integration of the PVD implanted in the full thickness skin defect model, although subcutaneous implantation model holds ideal features to investigate the potential of the construct to encourage anastomosis

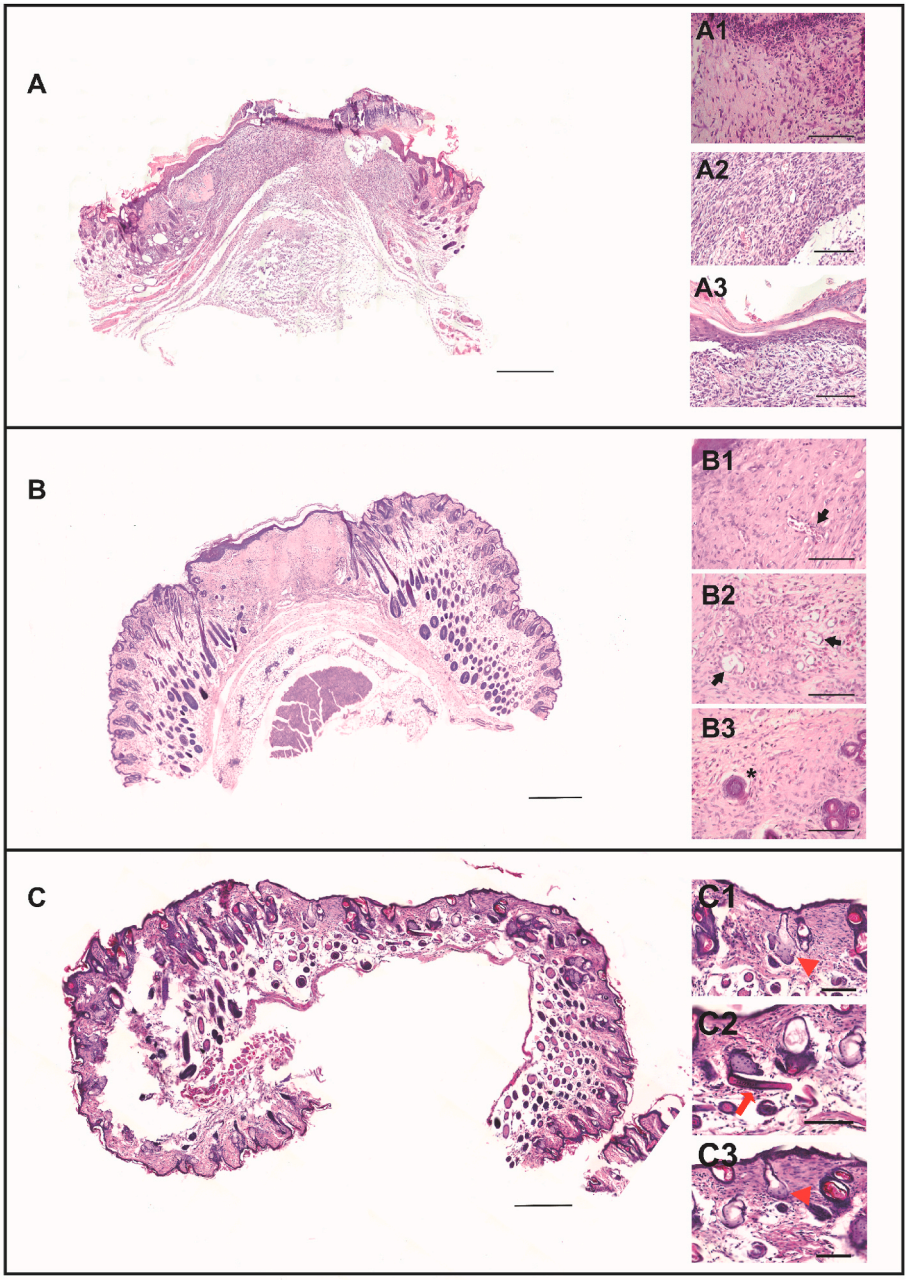

Fig. 2. Histological analysis of graft sections showing the progressive integration of the graft with the host tissue over 7, 14, and 21 days post-implantation. A. Tile scans of the entire section at 7 days after implantation. A1. Higher magnification of the borders between the graft and the host tissue. A2. Initial reorganization of the connective tissue. A3. Re-epithelialization process. B. Tile scans of the entire section at 14 days after implantation. B1. Integration of the construct with the host tissue. B2. Conspicuous ECM deposition made by cells recruited in the proximity of the implantation site along with the presence of blood vessels. B3. Follicle-like structures formation. C. Tile scans of the entire section at 21days after implantation. C1–C3. Newly formed perfused blood vessels within the graft and intermingled with sebaceous glands (yellow arrowheads) and hair shaft (yellow arrows). Dotted red arrows in the wide-field tile-scan images indicate the boundary between the implants and the surrounding healthy skin. Scale bars are: 250 μm in A, B and C; 50 μm in B1; 25 μm in A1, A2, B2, C1, C2 and C3.

onset by facilitating the development of functional connections from all sides of the implant. The better performance displayed by our engineered tissue when implanted in the full thickness skin defect model is probably due to the stromal and epithelial continuity guaranteed by this more physiological model. As shown in Fig. 1F–H, the PVD perfectly sustained the suture, indicating an adequate overall resistance comparable to that of the host skin. More interestingly, it supported the entire process of wound healing as displayed in Fig. 1I–N. Showcasing cell survival in vivo, we have presented macroscopic images within Fig. 1, showing the progressive evolution of wound healing from the initial placement of the skin substitute to its complete integration with the host tissue. Indeed, the significant reduction of the wound size over time after implantation demonstrated an effective integration of the PVD into the mouse skin and the following healing. The possibility to easily suture the graft witnesses the high translational potential held by the construct. Macroscopic observations revealed a well-integrated construct in the skin of all animals, without signs of adverse reaction. From 7 days onward (Fig. 1L–N) the suture was no longer necessary being the construct firmly adherent to the host tissue.

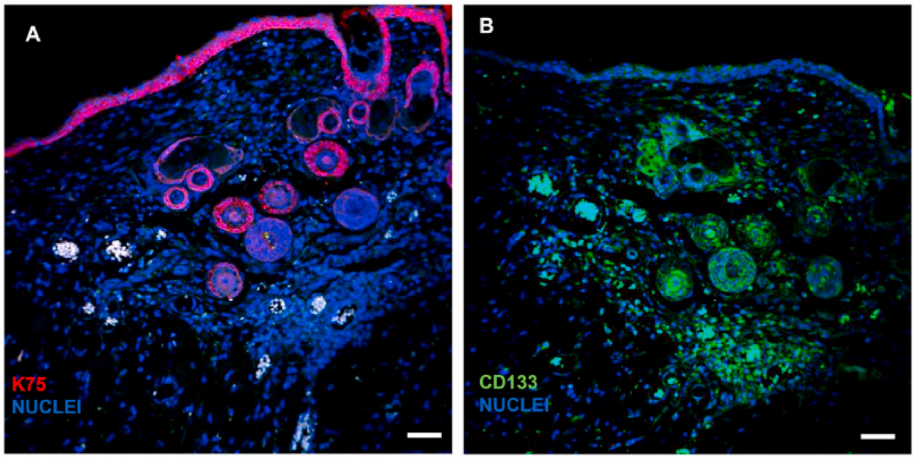

Fig. 3. Immunolabelling of hair follicle morphogenesis in the wounded region 14 days after implantation. A. Immunolabeling of K75 (red) in cells of hair bulbs; B. Immunolabelling of CD133 (green) in hair bulbs and surrounding stromal cells. Nuclei are counterstained with DAPI (blue). Scale bars are: 100 μm.

3.2. In vivo tissue integration: re-epithelialization and skin appendage formation

Microscopic evaluation of constructs at 7-, 14-, and 21-days post implantation were performed to i) confirm the PVD integration with the host wounded tissue; ii) assess the host tissue response to regeneration. In Fig. 2 and Supplementary Fig. S4, comprehensive tile scans of the entire sections revealed a uniform integration of the skin substitute with the host tissue, highlighting at the same time the absence of necrotic areas. Morphological analysis at precocious time points, i.e., 3 days after implantation (Supplementary Fig. S4 A). closely resembles the highly cellularized granulation tissue which stems from the exudate, featuring the first inflammatory phase of a physiological wound healing [39]. In Fig. S3_A1 the boundaries of the wound after 3 days are shown along with a clear recruitment of tissue-regenerating cells. In Fig. S3_A2 cells interspersed in a loose connective tissue in the wound region are clearly visible. Immunofluorescence images in the Supplementary Fig. S4 displays CD68 positive cells in the tissue at each time point. The presence of macrophages, marked by anti-CD68 immunostaining, disseminated in the tissue persisted up to the 7th day after implantation before decreasing. This trend witnesses the physiological evolution of the exudate during wound healing, without the need of specific treatments as well as washing, cleaning or bandaging of the wound area. In the light of these results, we can assume that on day 3 post-implantation an active wound healing process was set. A clear rearrangement of the tissue as a result of active cellular proliferation is detectable 7 days after implantation (Fig. 2 A, A1-A3) with the reorganization and the maturation of the newly formed connective tissue (Fig. 2 A2). This feature further indicates that a correct regenerative process occurs within the first week after implantation along with the epithelialization on the surface of the implanted construct (Fig. 2 A3). The graft-host interaction is observed after 14 days of implantation with a completely healed wound and full integration of the graft showing the same thickness of the surrounding host tissue (Fig. 2B). Newly formed blood vessels are evident at higher magnification (Fig. 2 B1–B2) indicating a consistent angiogenic process. Remarkably, at this stage structures that morphologically resemble hair follicles (Fig. 2 B3) further corroborate the observation of complete integration between the graft and the host tissue being the development of skin appendages far from a foregone datum. At 21 days after implantation, the graft appears fully integrated in the host tissue (Fig. 2C) Abundance of skin appendages including sebaceous glands (Fig. 2 C1–C3), not erupted hair shaft (Fig. 2 C2) are clearly visible, as well as a physiological connection between the hair shaft and the sebaceous glands (Fig. 2 C2). The host skin is thus featured by the massive presence of hair bulbs facilitating the recruitment of cells underlying the development of skin appendages by PVD [12]. Immunostaining against K75 and CD133 was performed at 14 days after implantation to further confirm hair follicle structure. K75 in hair bulb and germinative epithelial layer of the wound region (Fig. 3A) while CD133 labeling is detected in hair bulbs and surrounding stromal cells embedded in the ECM (Fig. 3B). Both markers are signs of undifferentiated hair follicle cells, in particular K75 is closely associated to epithelial and outer root sheath cell phenotype [40] while CD133 is associated to dermal papilla cells [41,42]. The positivity for these two markers indicates that PVD is able to promote hair follicle morphogenesis already 14 days after implantation [12]. After 21 days, the expression of K75 and CD133 was still detectable in the wound area but it was higher in the appendages than in the epithelium compared to day 14 (Supplementary Fig. S5 A,B). A similar signal was observed in the mouse skin used as control (Supplementary Fig. S5 C,D). The ability of a dermal substitute to sustain the development of host skin appendages such as sebaceous glands and hair follicles is critical to the full recovery of host skin function [11]. The morphogenesis of host skin appendages in PVD is promoted by a complex and well-organized ECM exhibiting structural and functional molecules. These latter guarantee a physiological spatio-temporal presentation of specific moieties that guide cells toward the accomplishment of a physiological morphogenesis including the formation of skin appendages. This hypothesis is sustained by our previous studies in which hair follicle-like morphogenesis occurred in vitro in a similar engineered model without the addition of stem cells [43]. In general, artificial skin substitutes fail to reconstruct skin appendages such as hair follicles, sweat and sebaceous glands. Since the lack of such elements strongly impairs the functionality of the skin and, in turn, patients' quality of life, the use of various types of stem cells and differentiation inducers have been explored to promote skin appendages formation [11]. In this regard, the transplantation of skin organoids derived from human pluripotent stem cells has proven successful in generating hairy-skin after grafting onto nude mice) [44]. Despite a moderate degree of success, the use of stem cells is limited by the lack of a deep understanding of the process and the control of their differentiation towards the desired specific tissue lineage, not to mention the ethical aspects [11]. Therefore, the possibility to obtain a functional skin substitute by using patient-derived somatic cells paves the way to a more feasible clinical translation.

3.3. Early and functional innervation of the skin graft

It was widely demonstrated that a pre-vascular network developed into a bioengineered construct can anastomose with host vessels and support tissue integration in vivo [13,45–47]. Unlike the vascular

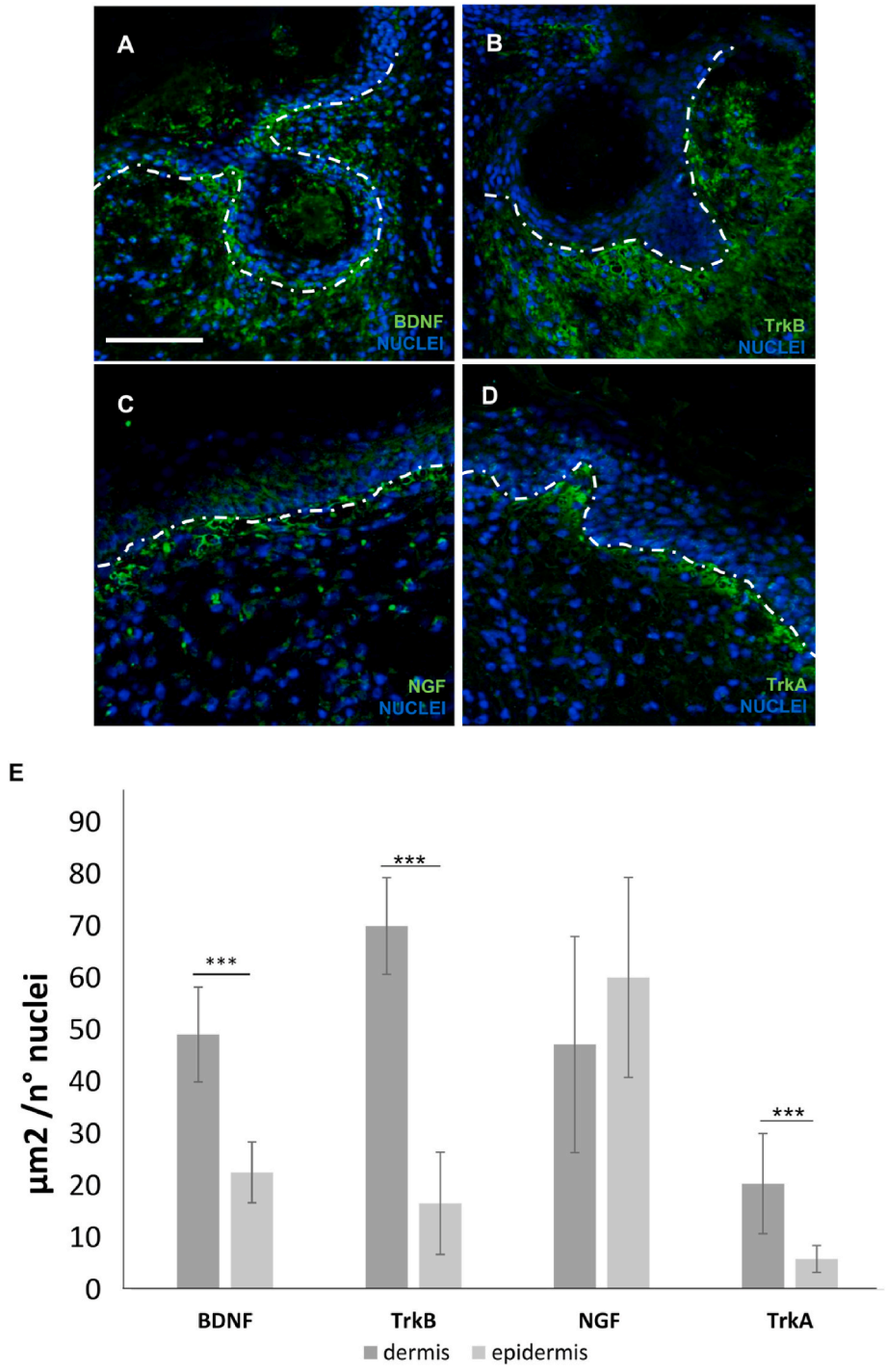

Fig. 4. BDNF, TRKB, NGF, and TrkA (green) immunofluorescent staining of engineered dermis retrieved 14 days after implantation (n = 3). Nuclei are counter-stained with DAPI (blue). A/D. The white dotted line separate the epithelium (in the upper part of the image) from the dermis (on the bottom); A,B. High expression of BDNF and TRKB is displayed into the PVD matrix) C. NGF displays a high signal in particular into the basal layer keratinocytes; D. TRKA high expression is detected immediately below the epidermis as well as in the dermal papilla. Confocal microscopy analysis, 25X objective. E. the relative estimation of protein signal in um2 normalized to number of cells. The graphs report mean values ± standard deviation, *** indicate a p value < 0.001. Scale bar is: 50 µm.

network, there is still no proof that a neural network created in vitro can connect with the host one. Despite the numerous efforts to obtain a pre-innervated construct in vitro [34,48,49], their application in vivo is always scarcely effective. Therefore, the implanted constructs are not provided with neural network, thus depending on the host induced innervation to integrate with native nerves [50,51]. Such reinnervation process involves the release of neurotrophic growth factors such as NGF and BDNF by keratinocytes and fibroblasts and the activation of their TRK receptors to promote neural cell survival, growth, differentiation, and migration. In this scenario, to assess the potential of PVD in promoting the formation of a neuronal network, we started by investigating the presence of BDNF and NGF and their high affinity receptors, respectively TRKB and TRKA, 14 days post-implantation. We observed a high expression of BDNF (Fig. 4A) and TRKB (Fig. 4B) in the dermis of the implanted PVD as well as in the basal layer of the epidermis. In accordance with the literature, the high production of BDNF in the

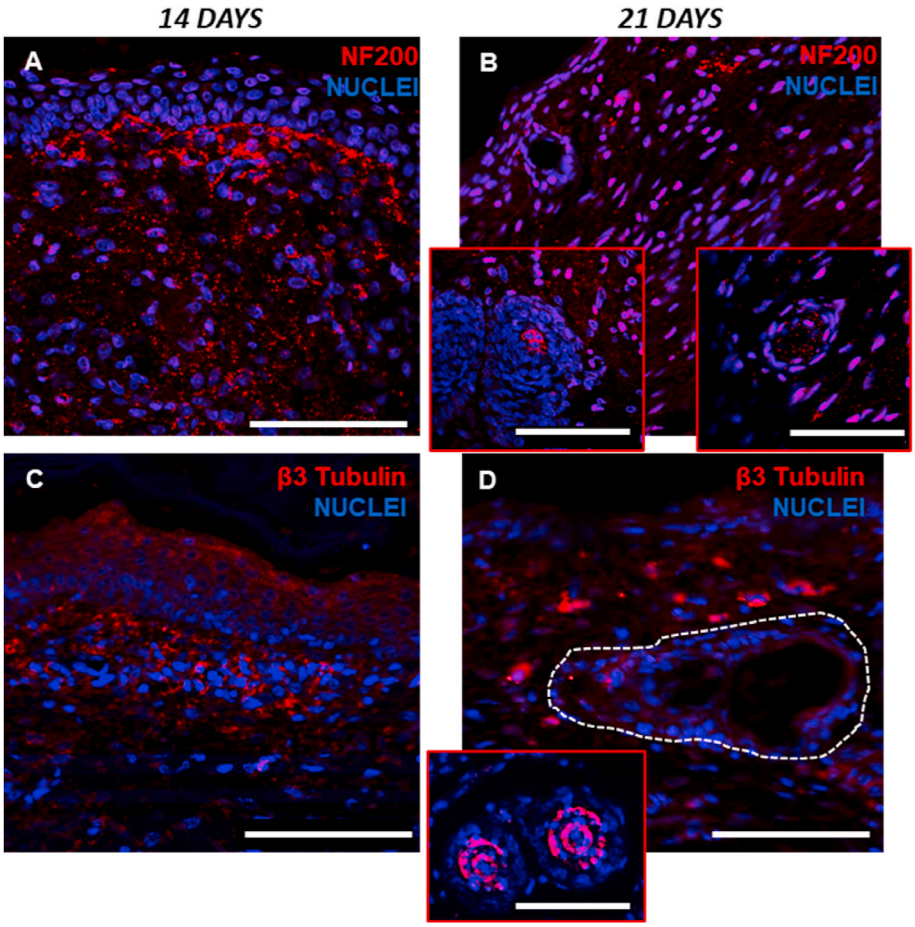

Fig. 5. Immunofluorescence staining for NF 200 and B3 Tubulin on engineered dermis retrieved 14- and 21-days post-implantation. A, B. NF200 immunolabeling (red) shows a high expression of the neural marker into the PVD matrix as well as in cutaneous appendages as highlighted in the red boxes. C, D. B3 Tubulin immunostaining (red) displays a clear signal of the early neural marker under and within the epidermal layer. Nuclei are counterstained with DAPI. The white dashed line marks a cutaneous gland structure in the PVD. Scale bar is: 100 μm.

dermis is correlated to the migration and formation of the tubular structures of endothelial cells [52,53]. During wound healing, the BDNF secreted by fibroblasts acts not only as neurotrophic factor, but it also increases the expression of β-actin and F-actin enhancing their differentiation into myofibroblasts [54,55]. Moreover, we observed a high expression of NGF in the basal layers of epidermis and in the upper dermis immediately below the epidermis (Fig. 4C) as result of the occurring re-epithelialization. In agreement with the literature, keratinocyte-derived NGF is a strong signal guiding skin re-innervation [56]. As expected, we found a high expression of the TRKA, the highest affinity NGF receptor, in fibroblasts situated at the dermal-epidermal junction (Fig. 4D). According to Fig. 2A the re-epithelialization occurred as early as 7 days after implantation. At this time point we did not detect neither neurotrophins nor their receptors, however, the ongoing epithelialization allowed to establish a correct signal for wound healing and re-innervation. Furthermore, to assess which compartment of the skin was mainly involved in the secretion of each neurotrophins and the expression of the related receptors, we compared the fluorescent signal displayed both by the epithelium and the dermis. The graphical representation (Fig. 4E) quantifies neurotrophins and their high affinity receptor distribution into the dermis and epidermis of the implanted PVD. Consistently with the literature, we found that BDNF and TRKB were more expressed into the dermis than the epidermis while NGF was more expressed into the latter [57]. In contrast, little or no signal was observed in epidermal keratinocytes and dermal fibroblasts at the not-wounded control skin sites, as confirmed also in Supplementary Fig. S6 showing the mislabelling of neurotrophins and their receptors in mouse tissue.

To clearly detect the neuronal network in PVD at 14 and 21 days after implantation we investigated the presence of the axonal marker neurofilament protein 200 KDa (NF200), which shows the presence of fiber neurons, and the Beta III tubulin (TUBB3), a protein that contributes to microtubule formation in neuronal cell bodies and axons. NF200 and TUBB3 immunostaining were performed also in the host skin, in a site far from the implant, as positive control confirming that the localization of the two markers (TUBB3 Supplementary Fig. S7 A, B and NF200 Fig. S7 C, D) in mouse skin was very similar to that detected in the implanted tissue. At 14 days post implantation we determined NF 200 immuno-positive fibers (Fig. 5A) in the dermis but not in the epidermis, indicating that the identified nerve fibres were Aβ fibres. Indeed, we observed that NF200-immunoreactive fibres or branches approaching the epidermal layer but not crossing the dermo-epithelial junction. At 21 days we found densely packed, NF200 immuno-positive, extremely small-caliber fibers in cutaneous appendages, as highlighted in the red box (Fig. 5B). As indicated by the literature, NF200 is normally upregulated in all pre-myelinated fibers during development and only persists in mature Aδ and Aβ fibers that become myelinated [58]. TUBB3 has been investigated as further structural peripheral neuronal marker playing a specific role in the rate of peripheral axon regeneration [59]. We found a strong signal in the dermis and intraepidermal compartments, particularly 14 days after implantation when thin fibers positive to TUBB3 were observed parallel to the derma-epidermal junction. Further, 21 days after implantation the signal was detected in the dermis close to the cutaneous appendage of

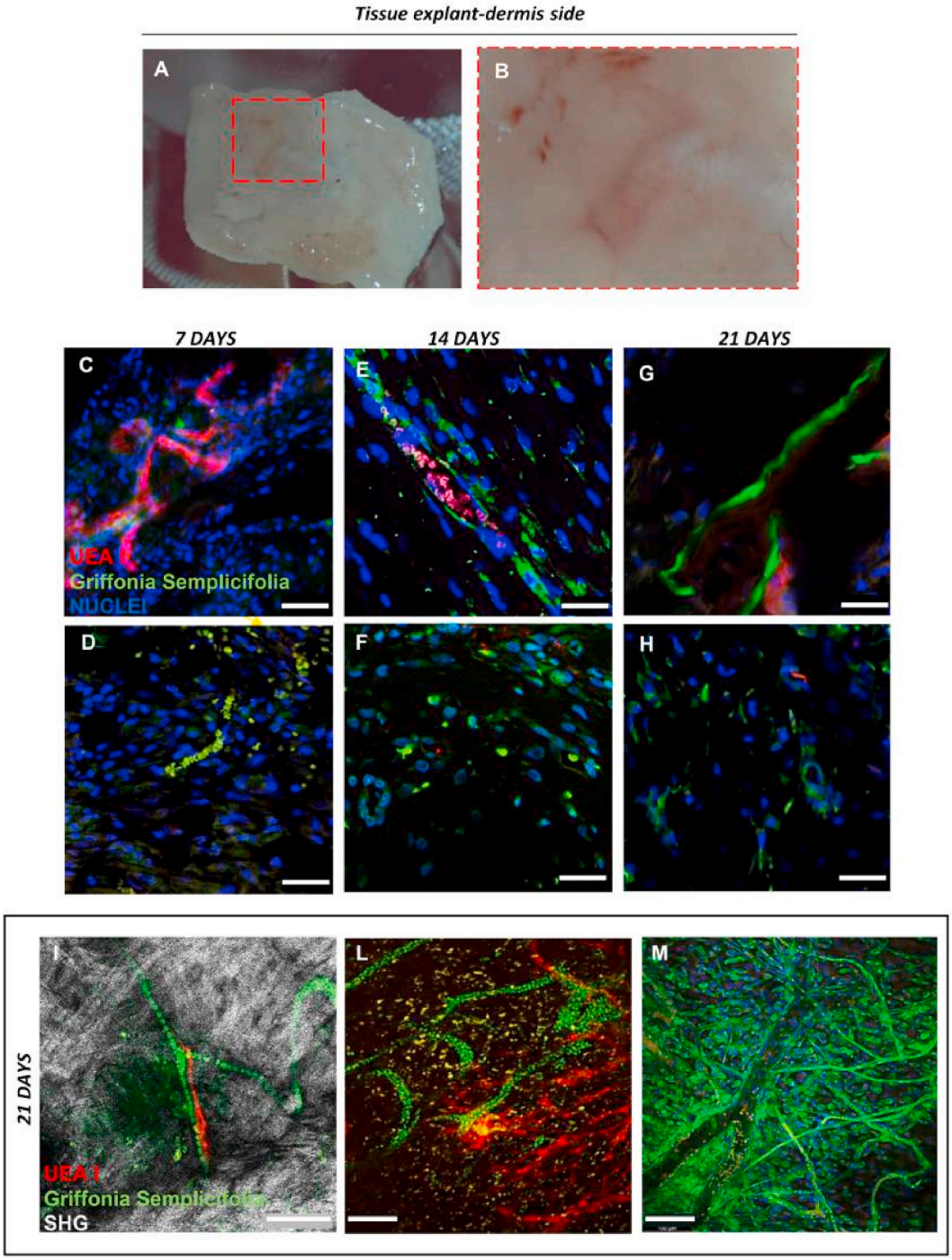

Fig. 6. Identification of endothelial structures in the tissue explanted at days 7, 14, 21 post-implantation. A. Macroscopic picture of the explant at day 7 post-implantation; B. zoom on blood vessels in the dermal side of the retrieved tissue; C–H. Fluorescent staining for the human lectin Rho-UEAI (red) and the mouse lectin Griffonia Semplicifolia-488 (green); scale bar 25 μm; C–H. Lectin staining on tissue sections 7, 14 and 21 days post implantation respectively. I-M. Lectin staining on whole clarified samples explanted at day 21 post-implantation showing collagen marked in grey by SHG imaging, human vessels from the PVD marked in red by Rho-UEAI and murine vessels in green by Griffonia Semplicifolia-488. Nuclei are counterstained with DAPI; scale bars are: in C–H 25 μm, in I 50 μm, in L-M 100 μm.

the implanted PVD (Fig. 5C and D). Both axon markers investigated at the two time points were characterized by small and dense cluster dots indicating the presence of nerve fibers even if during an early morphogenesis process. The signal displayed 14 and 21 days post implantation and its similarity to that expressed by the axonal marker NF200 in the host tissue, further highlights that a reinnervation process was effectively occurring in the PVD (Supplementary Fig. S7). Moreover, in the PVD explanted after 14 days, we also identified fibers showing immunopositivity for the neurofilament-M (NF-M) (Fig. S7). Taken together the neuronal marker analyses highlighted that innervation occurred in the PVD very early in comparison to the longer periods of time reported in the literature [26,51,60]. Indeed, one of the first example of functional innervation was reported by English et al. who used an autologous skin equivalent from adult rat implanted after 3 weeks of culture [60] showing the re-innervation of the engrafted tissue 83 days after implantation. More recently, Biedermann et al. displayed

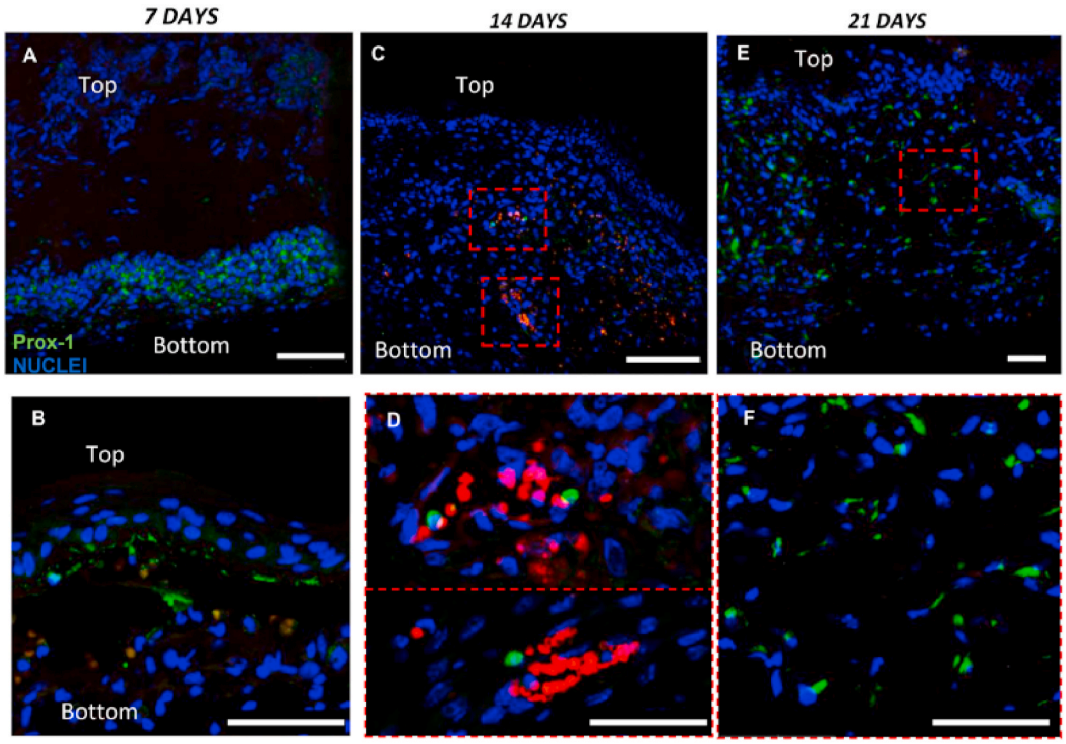

Fig. 7. Immunodetection of Prox1 in the implanted PVD Tissue sections at days 7 (A, B), 14 (C, D), and 21 (E, F) post-implantation marked by Prox1 (green); C, D. Localization of Prox1 positive cells nearby perfused blood vessels (the red autofluorescence highlights red blood cells into the vessel lumen); In A, B, C, E *top* and *bottom* indicate the upper (exposed to the air) and lower part (in contact with the murine tissue) of the implanted tissue Nuclei are counterstained with DAPI; scale bars are 50 μm.

re-innervation of a bioengineered skin equivalent in rats 8 weeks after implantation [51]. The same group demonstrated the persistence of myelinated and unmyelinated peripheral nerves in human skin substitutes up to 15 weeks after implantation in a full-thickness skin wound model in rat. In this case the bioengineered skin equivalent was made of a collagen I hydrogel populated by human primary cells [26]. Further, it is widely recognized that blood vessels play a role in guiding host-derived innervation. Indeed, several pieces of evidence underline that vascularization occurs before innervation stimulating nerve regeneration and recovery [61]. In addition, differentiated epithelium and structured ECM are known to be involved in neural recruitment and innervation [12,62]. Therefore, we can argue that the early innervation of the PVD occurring in only 14 days may be due to the presence of a pre-assembled ECM which includes a pre-vascular network. In the same context, the fast in vivo re-epithelialization is a key event which guarantees the spatial-temporal release of neurotrophic factors that stimulate tissue innervation in a very short time.

3.4. Vascular network and lymphatic marker localization in the skin graft

The efficiency of graft integration with the host tissue depends on several factors, among which the presence of a functional vascular and lymphatic network is crucial to guarantee tissue feeding and fluid homeostasis. The histological analysis reported in Fig. 2 was complemented by immunostaining reported in Fig. 6, displaying the development of a robust capillary network. These features confirm the viability and function of the cells included in our engineered skin substitute, further supporting the evidence of its successful integration within the host tissue. Tissue explants were analyzed to evaluate the presence of a functional vascular network able to sustain construct engraftment over time up to 21days. Lymphatic endothelial cells were also detected at the same time points. Macroscopic pictures in Fig. 6A and B shows the presence of perfused capillaries visible on the dermis side already 7 days post-implantation. The species-specific lectins Rho-Ulex-Europeaus-Agglutinin 1 (UEA-1) and FITC-Griffonia Semplicifolia were used to mark human and mouse vessels, respectively. After 7 days, both human (Fig. 6C) and murine (Fig. 6D) vessels were visible in the tissue sections. We observed the clear presence of auto-fluorescent red blood cells in the murine vessels (Fig. 6D), displaying their characteristic biconcave disc shape. At days 14 (Fig. 6E and F) and 21 (Fig. 6G and H), vessels of mouse origin were identified in the tissue slices. To better visualize the 3D vascular network, the whole samples stained with the lectins were clarified and observed by multiphoton and confocal microscopy. Fig. 6I highlights a close interaction between murine and human vessels in the collagenous matrix indicating that the primary human network probably played a role in the guidance of murine endothelial cells during tissue invasion and angiogenesis. At the same time, the observation of the whole 3D sample allowed us to identify the persistence of the human endothelial network up to 21 days after implantation (Fig. 6I and L). Furthermore, these vessels were not perfused and seemed to go toward a regression as indicated by the absence of auto-fluorescent red blood cells in the lumen along with the thinning of the red capillaries (lower than 10 μm in diameter) (Fig. 6L). Also, the green murine network resulted in completely perfused vessels with different diameters ranging from 10 to 40 μm (Fig. 6M).

Prox1 immunodetection was used to determine whether the lymphatic endothelial component was detectable within the implanted tissue. Prox1 is a transcription factor involved in many developmental and morphogenetic processes used to mark lymphatic endothelial cells, it is mainly localized in the nucleus but is detectable also in the cytoplasm [63]. After 7 days, Prox1 signal was detected on the bottom of the implanted tissue (Fig. 7A), but also close to the basal lamina of the epithelium (Fig. 7B) indicating the migration of Prox1 positive cells into the construct both from its top and bottom surfaces while 7 days later, on day 14 post-implantation, Prox1 positive cells were observed close to the blood vessels (Fig. 7C and D). It is known that Prox1 is expressed by a

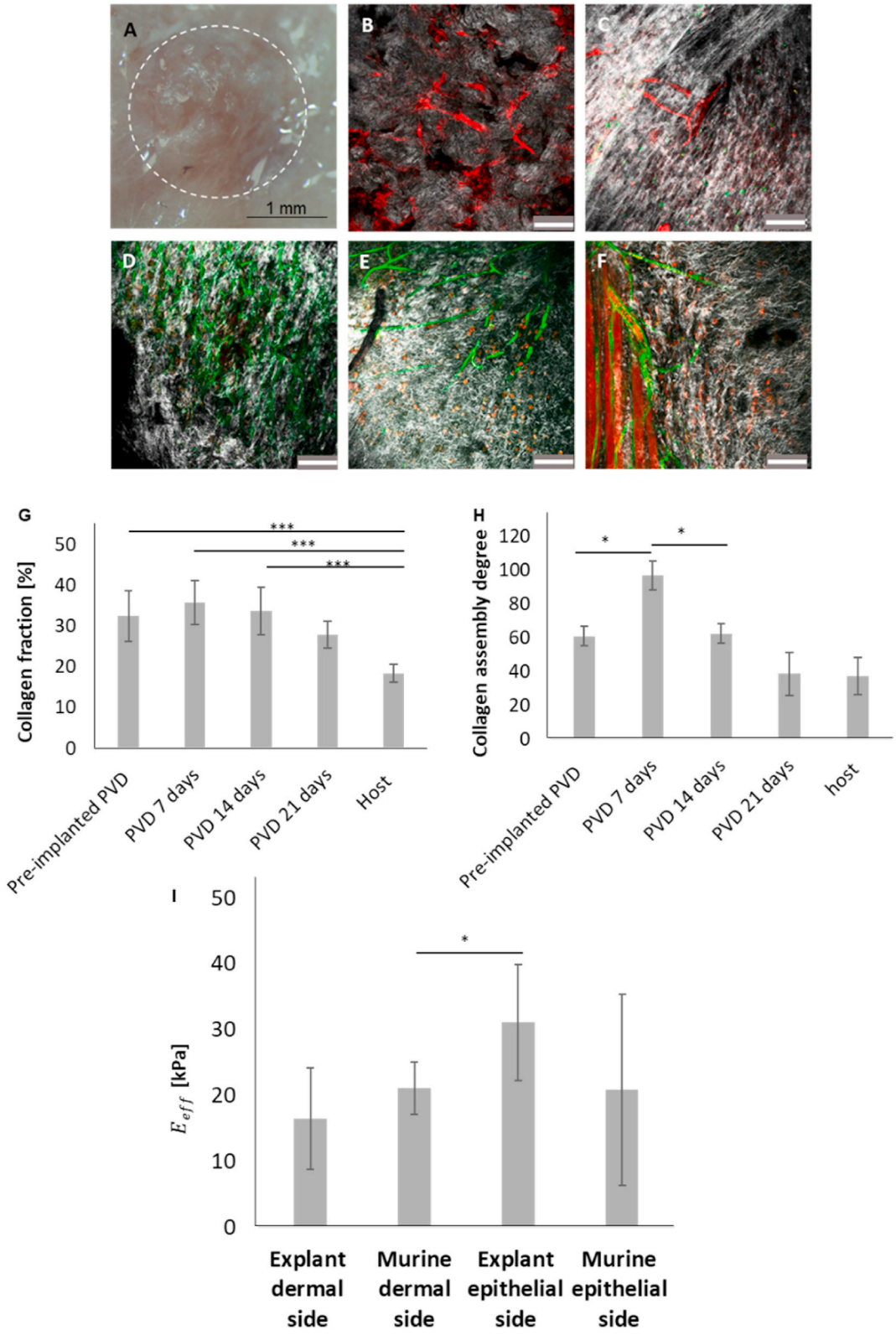

Fig. 8. Collagen structural analysis of the explanted tissue. A. Macroscopic image of the tissue explanted 7 days post-implantation. The dashed white circle highlights the presence of blood vessels; B. human capillaries marked by UEAI-Rho (red) within the PVD before implantation, scale bar respectively; F. Mouse capillaries marked by Griffonia Semplicifolia-488 (green) C–F. Scale bar 50 μm; G. Collagen fraction (%) measured before implantation and after 7, 14, and 21 days. Skin mouse has been used as control tissue; H. Collagen assembly degree (CAD) before implantation and after 7, 14, and 21 days mouse skin has been used as control tissue; I. Effective (or reduced) Young's modulus (E_{eff}) [kPa] of tissues explanted 21 days post-implantation compared to the epidermal and dermal sides of murine skin used as control. The graphs report mean values ± standard deviation, *p value < 0.05; ***pvalue<0.001. N = 3.

sub-population of endothelial cells that, after budding from blood vessels, originate lymphatic vessels [64]. Prox1 is not only responsible for the induction of lymphangiogenesis but also for the maintenance of a functional lymphatic network [65] Later, the distribution of Prox1 positive cells became more uniform over the tissue so that, on day 21 post-implantation, Prox1 signal increased showing a more linear distribution exactly as it happens to endothelial cells when they align themselves forming the vessels.

3.5. Collagen and vascular network evolution in the skin graft

The final step of the wound healing process is tissue remodelling which leads to the formation of a highly organized collagen matrix whose structure closely mimics the native tissue. In this phase, fibroblasts play a pivotal role in degrading and secreting ECM components to produce changes in collagen quantity and organization, thus enhancing tissue tensile strength. This process usually occurs over a long time beginning in 2/3 weeks and lasting years [66,67]. Surprisingly, a rapid remodelling of collagen fibers was observed in the implanted PVD where the architecture of collagen resembled the murine tissue in only 21 days. We used second harmonic multiphoton (SHG) microscopy to observe collagen structure in tissue harvested after 7, 14 and 21 days in comparison to the in vitro PVD and the murine skin. Although the position of the PVD in the explanted tissue was macroscopically clear (Fig. 8A), we used human/murine vessels for a more precise, microscope-driven localization of the construct. In Fig. 8B/F human capillaries were marked in red by UEA-I, murine vessels in green by Griffonia Simplicifolia, and the collagen in grey by the second harmonic generation signal (SHG). Fig. 8B shows the PVD in vitro, Fig. 8C/E the tissue explanted 7, 14 and 21 days after implantation whereas Fig. 8F shows the murine tissue. The latter was identified via hair auto fluorescence (in red) (Fig. 8F). The PVD already in vitro was featured by the presence of collagen being produced by human dermal fibroblasts during the bioengineering process that ultimately culminated in the production of the 3D bioengineered dermis. The ECM of PVD presented differences in comparison to the murine one in terms of collagen fraction (Fig. 8G) but not of assembly degree (Fig. 8H). The difference in collagen fraction between the PVD and murine tissue may be due to the human source of tissue and the in vitro production of the matrix. The collagen fraction of the PVD progressively approached the corresponding value in the murine tissue 21 days after implantation (Fig. 8G). The degree of collagen assembly changed from the in vitro condition to the tissue harvested 7 days post-implantation, probably in concomitance with the proliferative phase of wound healing, during which fibroblasts assemble collagen fibers and keratinocyte migration occurs [68]. Afterwards, the collagen assembly degree in the wound area resembled the murine one (Fig. 8H). These data demonstrated that the PVD, thanks to the pre-assembled matrix, speeded up the process of tissue remodelling by developing in just 21 days a mature tissue structurally and mechanically similar to the host one. At this time point, the E_{eff} of the explant measured on the dermis side was very close to the murine one while the mechanical properties of the epithelial side were slightly higher than those of the murine tissue, however, this difference was not statistically relevant (Fig. 8I). These data demonstrated that the PVD experienced an effective tissue remodelling over time leading to the mimicry of the murine skin in terms of collagen quantity and E_{eff}.

4. Conclusion

Over the last decades many efforts have been addressed to design the optimal scaffold to generate skin substitutes by attempting to resemble the composition of normal skin to enhance clinical effectiveness [69]. Among the several strategies proposed, the one based on the production of dermal equivalents composed of fibroblast-derived dermal matrix in which cells deposit their own ECM represents the more promising to generate functional substitutes. In this context the cell microenvironment of the native ECM along with its regulatory/instructive and repository role is preserved allowing the replication of key morphogenetic events (i.e., hair follicle generation, innervation, vascularization). The development of these morphological features would be otherwise depressed as it happens when exogenous scaffolds are used as ECM surrogates. In this scenario, our work demonstrates the unparallel capability of PVD to treat full thickness wounds by guarantying a rapid, effective, and functional skin healing. Our results, confirm that PVD sustains a rapid host vasculature invasion, angiogenesis and re-epithelialization (7 days post implantation). This revealed the capacity of the PVD to attract peripheral host nerve fibres in a very short time never observed before (14 days post implantation). In addition, both lymphatic vessels and skin appendages, such as follicle and sebaceous glands, were observed at the implantation site (14 days post implantation). Taken together, these results demonstrate an astonishing behaviour of this dermis model in promoting the plethora of key biological processes leading to a complete wound repair and tissue regeneration. The rapid ingrowth of neuro-vascular structures as well as of lymphatic vessels into the skin grafts along with the development of skin appendages favourably impact the clinical application of the proposed engineered tissue.

CRediT authorship contribution statement

Claudia Mazio: Writing - original draft, Software, Methodology, Investigation. **Isabella Mavaro:** Writing - original draft, Software, Methodology, Investigation. **Antonio Palladino:** Software, Methodology, Investigation. **Costantino Casale:** Software, Methodology, Investigation. **Francesco Urciuolo:** Writing - review & editing, Formal analysis. **Andrea Banfi:** Writing - review & editing, Writing - original draft. **Livia D'Angelo:** Writing - review & editing, Formal analysis. **Paolo A. Netti:** Writing - review & editing, Resources, Funding acquisition. **Paolo de Girolamo:** Writing - review & editing, Resources, Funding acquisition. **Giorgia Imparato:** Writing - review & editing, Writing - original draft, Supervision, Conceptualization. **Chiara Attanasio:** Writing - review & editing, Writing - original draft, Supervision, Conceptualization.

Declaration of competing interest

The authors declare that they have no known competing financial interests or personal relationships that could have appeared to influence the work reported in this paper.

Data availability

Data will be made available on request.

Acknowledgment

We acknowledge funding received from: 899822 SOMA FETOPEN-01-2018-2019-2020 FET-Open Challenging Current Thinking; Biorobotics Research and Innovation Engineering Facilities – IR0000036 BRIEF PNRR MUR; FIT4MEDROB: Fit for Medical Robotics- PNRR MUR (PNC0000007).

Appendix A. Supplementary data

Supplementary data to this article can be found online at https://doi.org/10.1016/j.mtbio.2024.100949.

References

[1] Á. Sierra-Sánchez, K.H. Kim, G. Blasco-Morente, S. Arias-Santiago, Cellular human tissue-engineered skin substitutes investigated for deep and difficult to heal injuries, Npj Regen. Med. 61 (6) (2021) 1–23, https://doi.org/10.1038/s41536-021-00144-0.

[2] F. Groeber, M. Holeiter, M. Hampel, S. Hinderer, K. Schenke-Layland, Skin tissue engineering - in vivo and in vitro applications, Adv. Drug Deliv. Rev. 63 (2011) 352–366, https://doi.org/10.1016/j.addr.2011.01.005.

[3] A.W.C. Chua, Y.C. Khoo, B.K. Tan, K.C. Tan, C.L. Foo, S.J. Chong, Skin tissue engineering advances in severe burns: review and therapeutic applications, Burn. Trauma 4 (2016) 3, https://doi.org/10.1186/s41038-016-0027-y.

[4] S. Böttcher-Haberzeth, Thomas Biedermann, Ernst Reichman, Tissue engineering of skin, Burns 36 (2010) 450–460, https://doi.org/10.1016/j.burns.2009.08.016.

[5] R. Cai, N. Gimenez-Camino, M. Xiao, S. Bi, K.A. Divito, Technological advances in three-dimensional skin tissue engineering, Rev. Adv. Mater. Sci. 62 (2023) 1–22, https://doi.org/10.1515/rams-2022-0289.

[6] P. a Janmey, J.P. Winer, J.W. Weisel, Fibrin gels and their clinical and bioengineering applications, J. R. Soc. Interface 6 (2009) 1–10, https://doi.org/10.1098/rsif.2008.0327.

[7] X. Zhao, X. Sun, L. Yildirimer, Q. Lang, Z.Y. (William) Lin, R. Zheng, Y. Zhang, W. Cui, N. Annabi, A. Khademhosseini, Cell infiltrative hydrogel fibrous scaffolds for accelerated wound healing, Acta Biomater. 49 (2017) 66–77, https://doi.org/10.1016/J.ACTBIO.2016.11.017.

[8] H. Fu, D. Zhang, J. Zeng, Q. Fu, Z. Chen, X. Sun, Y. Yang, S. Li, M. Chen, Application of 3D-printed tissue-engineered skin substitute using innovative biomaterial loaded with human adipose-derived stem cells in wound healing, Int. J. Bioprinting 9 (2022) 394–406, https://doi.org/10.18063/IJB.V9I2.674.

[9] M.T. Cerqueira, R.P. Pirraco, a.R. Martins, T.C. Santos, R.L. Reis, a.P. Marques, Cell sheet technology-driven re-epithelialization and neovascularization of skin wounds, Acta Biomater. 10 (2014) 3145–3155, https://doi.org/10.1016/j.actbio.2014.03.006.

[10] B.L. Dearman, S.T. Boyce, J.E. Greenwood, Advances in skin tissue bioengineering and the challenges of clinical translation, Front. Surg. 8 (2021) 1–10, https://doi.org/10.3389/fsurg.2021.640879.

[11] T. Weng, P. Wu, W. Zhang, Y. Zheng, Q. Li, R. Jin, H. Chen, C. You, S. Guo, C. Han, X. Wang, Regeneration of skin appendages and nerves: current status and further challenges, J. Transl. Med. 181 (18) (2020) 1–17, https://doi.org/10.1186/S12967-020-02248-5.

[12] F. Urciuolo, C. Casale, G. Imparato, P.A. Netti, Bioengineered skin substitutes: the role of extracellular matrix and vascularization in the healing of deep wounds, J. Clin. Med. 8 (2019), https://doi.org/10.3390/JCM8122083.

[13] C. Mazio, C. Casale, G. Imparato, F. Urciuolo, C. Attanasio, M. De Gregorio, F. Rescigno, P.A. Netti, Pre-vascularized dermis model for fast and functional anastomosis with host vasculature, Biomaterials 192 (2019) 159–170, https://doi.org/10.1016/j.biomaterials.2018.11.018.

[14] M. Jafari, Z. Paknejad, M.R. Rad, S.R. Motamedian, M.J. Eghbal, N. Nadjmi, A. Khojasteh, Polymeric scaffolds in tissue engineering: a literature review, J. Biomed. Mater. Res. B Appl. Biomater. 105 (2017) 431–459, https://doi.org/10.1002/JBM.B.33547.

[15] N. Annabi, D. Rana, E. Shirzaei Sani, R. Portillo-Lara, J.L. Gifford, M.M. Fares, S. M. Mithieux, A.S. Weiss, Engineering a sprayable and elastic hydrogel adhesive with antimicrobial properties for wound healing, Biomaterials 139 (2017) 229–243, https://doi.org/10.1016/J.BIOMATERIALS.2017.05.011.

[16] Y. Li, C. Zou, J. Shao, X. Zhang, Y. Li, Preparation of SiO2/PS superhydrophobic fibers with bionic controllable micro–nano structure via centrifugal spinning, RSC Adv. 7 (2017) 11041–11048, https://doi.org/10.1039/C6RA25813A.

[17] H. Matsumine, H. Fujimaki, M. Takagi, S. Mori, T. Iwata, M. Shimizu, M. Takeuchi, Full-thickness skin reconstruction with basic fibroblast growth factor-impregnated collagen-gelatin sponge, Regen. Ther. 11 (2019) 81–87, https://doi.org/10.1016/J.RETH.2019.06.001.

[18] H. Hu, F.J. Xu, Rational design and latest advances of polysaccharide-based hydrogels for wound healing, Biomater. Sci. 8 (2020) 2084–2101, https://doi.org/10.1039/D0BM00055H.

[19] P.W. Andrews, Pwa, Human pluripotent stem cells: tools for regenerative medicine, Biomater. Transl. 2 (2021) 294–300, https://doi.org/10.12336/BIOMATERTRANSL.2021.04.004.

[20] K.H. Bouhadir, D.D.J. Mooney, Promoting angiogenesis in engineered tissues, J. Drug Target. 9 (2001) 397–406, https://doi.org/10.3109/10611860108998775.

[21] Y. Yao, C. Wang, Dedifferentiation: inspiration for devising engineering strategies for regenerative medicine, Npj Regen. Med. 51 (5) (2020) 1–11, https://doi.org/10.1038/s41536-020-00099-8.

[22] M.W. Laschke, M.D. Menger, Prevascularization in tissue engineering: current concepts and future directions, Biotechnol. Adv. 34 (2016) 112–121, https://doi.org/10.1016/J.BIOTECHADV.2015.12.004.

[23] L. Chen, Q. Xing, Q. Zhai, M. Tahtinen, F. Zhou, L. Chen, Y. Xu, S. Qi, F. Zhao, Pre-vascularization enhances therapeutic effects of human mesenchymal stem cell sheets in full thickness skin wound repair, Theranostics 7 (2017) 117–131, https://doi.org/10.7150/THNO.17031.

[24] T. Biedermann, A.S. Klar, S. Böttcher-Haberzeth, C. Schiestl, E. Reichmann, M. Meuli, Tissue-engineered dermo-epidermal skin analogs exhibit de novo formation of a near natural neurovascular link 10 weeks after transplantation, Pediatr. Surg. Int. 30 (2014) 165–172, https://doi.org/10.1007/S00383-013-3446-X/FIGURES/4.

[25] T. Biedermann, S. Böttcher-Haberzeth, A.S. Klar, L. Pontiggia, C. Schiestl, C. Meuli-Simmen, E. Reichmann, M. Meuli, Rebuild, restore, reinnervate: Do human tissue engineered dermo-epidermal skin analogs attract host nerve fibers for innervation? Pediatr. Surg. Int. 29 (2013) 71–78, https://doi.org/10.1007/S00383-012-3208-1/FIGURES/6.

[26] T. Biedermann, A.S. Klar, S. Böttcher-Haberzeth, E. Reichmann, M. Meuli, Myelinated and unmyelinated nerve fibers reinnervate tissue-engineered dermo-epidermal human skin analogs in an in vivo model, Pediatr. Surg. Int. 32 (2016) 1183–1191, https://doi.org/10.1007/S00383-016-3978-Y/FIGURES/6.

[27] G. Imparato, F. Urciuolo, C. Casale, P.a. Netti, The role of microscaffold properties in controlling the collagen assembly in 3D dermis equivalent using modular tissue engineering, Biomaterials 34 (2013) 7851–7861, https://doi.org/10.1016/j.biomaterials.2013.06.062.

[28] F. Urciuolo, A. Garziano, G. Imparato, V. Panzetta, S. Fusco, C. Casale, P. Netti, Biophysical properties of dermal building-blocks affect extra cellular matrix assembly in 3D endogenous macrotissue, Biofabrication 8 (2016) 015010, https://doi.org/10.1088/1758-5090/8/1/015010.

[29] P. Yavvari, A. Laporte, L. Elomaa, F. Schraufstetter, I. Pacharzina, A.D. Daberkow, A. Hoppensack, M. Weinhart, 3D-Cultured vascular-like networks enable validation of vascular disruption properties of drugs in vitro, Front. Bioeng. Biotechnol. 10 (2022) 1–16, https://doi.org/10.3389/fbioe.2022.888492.

[30] R. Costa-Almeida, M. Gomez-Lazaro, C. Ramalho, P.L. Granja, R. Soares, S. G. Guerreiro, Fibroblast-endothelial partners for vascularization strategies in tissue engineering, Tissue Eng. - Part A 21 (2015) 1055–1065, https://doi.org/10.1089/ten.tea.2014.0443.

[31] A.F. Black, F. Berthod, N. L'Heureux, L. Germain, F.A. Auger, In vitro reconstruction of a human capillary-like network in a tissue-engineered skin equivalent, FASEB J. 12 (1998) 1331–1340, https://doi.org/10.1096/fasebj.12.13.1331.

[32] J. Wen, X. Li, X. Leng, X. Xu, X. Wu, An advanced mouse model for human skin wound healing, Exp. Dermatol. 26 (2017) 433–435, https://doi.org/10.1111/exd.13258.

[33] S. Böttcher-Haberzeth, Thomas Biedermann, Ernst Reichmann, Tissue engineering of skin, BURNS 36 (2010) 450–460, https://doi.org/10.1016/j.burns.2009.08.016.

[34] F. Martorina, C. Casale, F. Urciuolo, P.A. Netti, G. Imparato, In vitro activation of the neuro-transduction mechanism in sensitive organotypic human skin model, Biomaterials 113 (2017) 217–229, https://doi.org/10.1016/j.biomaterials.2016.10.051.

[35] C. Mazio, C. Casale, G. Imparato, F. Urciuolo, P.A. Netti, Recapitulating spatiotemporal tumor heterogeneity in vitro through engineered breast cancer microtissues, Acta Biomater. 73 (2018) 236–249, https://doi.org/10.1016/j.actbio.2018.04.028.

[36] C. Mazio, L.S. Scognamiglio, R. De Cegli, L.J.V. Galietta, D. Di Bernardo, C. Casale, F. Urciuolo, G. Imparato, P.A. Netti, Intrinsic abnormalities of cystic fibrosis airway connective tissue revealed by an in vitro 3D stromal model, Cells 9 (2020) 1–20, https://doi.org/10.3390/cells9061371.

[37] D.C. Lin, D.I. Shreiber, E.K. Dimitriadis, F. Horkay, Spherical indentation of soft matter beyond the Hertzian regime: numerical and experimental validation of hyperelastic models, Biomech. Model. Mechanobiol. 8 (2009) 345–358, https://doi.org/10.1007/s10237-008-0139-9.

[38] Z. Ostrowska-Podhorodecka, I. Ding, M. Norouzi, C.A. McCulloch, Impact of vimentin on regulation of cell signaling and matrix remodeling, Front. Cell Dev. Biol. 10 (2022) 562, https://doi.org/10.3389/FCELL.2022.869069/BIBTEX.

[39] M. Rodrigues, N. Kosaric, C.A. Bonham, G.C. Gurtner, Wound healing: a cellular perspective, Physiol. Rev. 99 (2019) 665–706, https://doi.org/10.1152/physrev.00067.2017.-Wound.

[40] A.L. Mesler, N.A. Veniaminova, M. V Lull, S.Y. Wong, Hair follicle terminal differentiation is orchestrated by distinct early and late matrix progenitors, Cell Rep. 19 (2017) 809–821, https://doi.org/10.1016/j.celrep.2017.03.077.Hair.

[41] L. Zhou, K. Yang, A. Carpenter, R.A. Lang, T. Andl, Y. Zhang, CD133-positive dermal papilla-derived Wnt ligands regulate postnatal hair growth, Biochem. J. 473 (2016) 3291–3305, https://doi.org/10.1042/BCJ20160466.CD133-positive.

[42] L. Zhou, M. Xu, Y. Yang, K. Yang, R.R. Wickett, Activation of β -catenin signaling in CD133- positive dermal papilla cells drives postnatal hair growth, PLoS Genet. (2016) 1–19, https://doi.org/10.1371/journal.pone.0160425.

[43] C. Casale, G. Imparato, F. Urciuolo, P.A. Netti, Endogenous human skin equivalent promotes in vitro morphogenesis of follicle-like structures, Biomaterials 101 (2016) 86–95, https://doi.org/10.1016/j.biomaterials.2016.05.047.

[44] J. Lee, C.C. Rabbani, H. Gao, M.R. Steinhart, B.M. Woodruff, Z.E. Pflum, A. Kim, S. Heller, Y. Liu, T.Z. Shipchandler, K.R. Koehler, Hair-bearing human skin generated entirely from pluripotent stem cells, Nature 582 (2020) 399–404, https://doi.org/10.1038/s41586-020-2352-3.

[45] D. Marino, J. Luginbühl, S. Scola, M. Meuli, E. Reichmann, Bioengineering dermo-epidermal skin grafts with blood and lymphatic capillaries, Sci. Transl. Med. 6 (2014) 221ra14, https://doi.org/10.1126/scitranslmed.3006894.

[46] L. Gibot, T. Galbraith, J. Huot, F. a Auger, A preexisting microvascular network benefits in vivo revascularization of a microvascularized tissue-engineered skin substitute, Tissue Eng. 16 (2010) 3199–3206, https://doi.org/10.1089/ten.tea.2010.0189.

[47] J.D. Baranski, R.R. Chaturvedi, K.R. Stevens, J. Eyckmans, B. Carvalho, R. D. Solorzano, M.T. Yang, J.S. Miller, S.N. Bhatia, C.S. Chen, Geometric control of vascular networks to enhance engineered tissue integration and function, Proc. Natl. Acad. Sci. U.S.A. 110 (2013) 7586–7591, https://doi.org/10.1073/pnas.1217796110.

[48] N. Lebonvallet, N. Boulais, C. Le Gall, U. Pereira, D. Gauché, E. Gobin, J.O. Pers, C. Jeanmaire, L. Danoux, G. Pauly, L. Misery, Effects of the re-innervation of organotypic skin explants on the epidermis, Exp. Dermatol. 21 (2012) 156–158, https://doi.org/10.1111/j.1600-0625.2011.01421.x.

[49] Q. Muller, M.J. Beaudet, T. De Serres-Bérard, S. Bellenfant, V. Flacher, F. Berthod, Development of an innervated tissue-engineered skin with human sensory neurons and Schwann cells differentiated from iPS cells, Acta Biomater. 82 (2018) 93–101, https://doi.org/10.1016/j.actbio.2018.10.011.

[50] S. Das, W.J. Gordián-vélez, H.C. Ledebur, F. Mourkioti, M.D. Serruya, D.K. Cullen, Innervation : the missing link for biofabricated tissues and organs, Npj Regen. Med. (2020), https://doi.org/10.1038/s41536-020-0096-1.
[51] T. Biedermann, A.S. Klar, S. Böttcher-Haberzeth, C. Schiestl, E. Reichmann, M. Meuli, Tissue-engineered dermo-epidermal skin analogs exhibit de novo formation of a near natural neurovascular link 10 weeks after transplantation, Pediatr. Surg. Int. 30 (2014) 165–172, https://doi.org/10.1007/s00383-013-3446-x.
[52] C. Sun, Y. Hu, Z. Chu, J. Huang, L. Zhang, The effect of brain-derived neurotrophic factor on angiogenesis, J. Huazhong Univ. Sci. Technolog. Med. Sci. 29 (2009) 139–143, https://doi.org/10.1007/S11596-009-0201-6.
[53] S. Matsuda, T. Fujita, M. Kajiya, K. Takeda, H. Shiba, H. Kawaguchi, H. Kurihara, Brain-derived neurotrophic factor induces migration of endothelial cells through a TrkB-ERK-integrin αVβ3-FAK cascade, J. Cell. Physiol. 227 (2012) 2123–2129, https://doi.org/10.1002/JCP.22942.
[54] J. Dudás, M. Bitsche, V. Schartinger, C. Falkeis, G. Mathias, H. Riechelmann, Fibroblasts produce brain-derived neurotrophic factor and induce mesenchymal transition of oral tumor cells, Oral Oncol. 47 (2011) 98–103, https://doi.org/10.1016/j.oraloncology.2010.11.002.
[55] E. Cherubini, S. Mariotta, D. Scozzi, R. Mancini, G. Osman, M.D. Ascanio, P. Bruno, G. Cardillo, A. Ricci, BDNF/TrkB axis activation promotes epithelial – mesenchymal transition in idiopathic pulmonary fibrosis, J. Transl. Med. (2017) 1–10, https://doi.org/10.1186/s12967-017-1298-1.
[56] H. Matsuda, H. Koyama, H. Sato, J. Sawada, A. Itakura, A. Tanaka, M. Matsumoto, K. Konno, H. Ushio, K. Matsuda, Role of nerve growth factor in cutaneous wound healing: accelerating effects in normal and healing-impaired diabetic mice, J. Exp. Med. 187 (1998) 297–306, https://doi.org/10.1084/jem.187.3.297.
[57] M. Ashrafi, M. Baguneid, A. Bayat, The role of neuromediators and innervation in cutaneous wound healing, Acta Derm. Venereol. 96 (2016) 587–597, https://doi.org/10.2340/00015555-2321/.
[58] F.L. Rice, G. Houk, J.P. Wymer, S.J.C. Gosline, J. Guinney, J. Wu, N. Ratner, M. P. Jankowski, S. La Rosa, M. Dockum, J.R. Storey, S.L. Carroll, P.J. Albrecht, V. M. Riccardi, The Evolution and Multi-Molecular Properties of NF1 Cutaneous Neurofibromas Originating from C-Fiber Sensory Endings and Terminal Schwann Cells at Normal Sites of Sensory Terminations in the Skin, 2019, https://doi.org/10.1371/journal.pone.0216527.
[59] A. Latremoliere, L. Cheng, M. Delisle, M.A. Tischfield, C.J. Woolf, E.C. Engle, Neuronal-specific TUBB3 is not required for normal neuronal function but is essential for timely axon regeneration, Cell Rep. 24 (2018) 1865–1879, https://doi.org/10.1016/j.celrep.2018.07.029.
[60] K.B. English, N. Stayner, G.G. Krueger, R.P. Tuckett, Functional innervation of cultured skin grafts, J. Invest. Dermatol. 99 (1992) 120–128, https://doi.org/10.1111/1523-1747.ep12616765.
[61] M. Snapyan, M. Lemasson, M.S. Brill, M. Blais, M. Massouh, J. Ninkovic, C. Gravel, F. Berthod, M. Götz, P. a Barker, A. Parent, A. Saghatelyan, Vasculature guides migrating neuronal precursors in the adult mammalian forebrain via brain-derived neurotrophic factor signaling, J. Neurosci. 29 (2009) 4172–4188, https://doi.org/10.1523/JNEUROSCI.4956-08.2009.
[62] N.C. Nowak, D.M. Menichella, R. Miller, A.M.Y.S. Paller, Cutaneous Innervation in Impaired Diabetic Wound Healing, 2021, https://doi.org/10.1016/j.trsl.2021.05.003.
[63] M. Rudzí Nska, M. Grzanka, A. Stachurska, M. Mikula, K. Paczkowska, T. Stępień, A. Paziewska, J. Ostrowski, B. Czarnocka, Molecular signature of Prospero Homeobox 1 (PROX1) in Follicular thyroid carcinoma cells, Int. J. Mol. Sci. Artic. (2019), https://doi.org/10.3390/ijms20092212.
[64] J.T. Wigle, N. Harvey, M. Detmar, I. Lagutina, G. Grosveld, M.D. Gunn, D. G. Jackson, G. Oliver, An essential role for Prox1 in the induction of the lymphatic endothelial cell phenotype, EMBO J. 21 (2002) 1505–1513, https://doi.org/10.1093/emboj/21.7.1505.
[65] N.C. Johnson, M.E. Dillard, P. Baluk, D.M. McDonald, N.L. Harvey, S.L. Frase, G. Oliver, Lymphatic endothelial cell identity is reversible and its maintenance requires Prox1 activity, Genes Dev. 22 (2008) 3282, https://doi.org/10.1101/GAD.1727208.
[66] A.C.D.O. Gonzalez, Z.D.A. Andrade, T.F. Costa, A.R.A.P. Medrado, Wound healing - a literature review, An. Bras. Dermatol. 91 (2016) 614–620, https://doi.org/10.1590/abd1806-4841.20164741.
[67] R.B. Diller, A.J. Tabor, The role of the extracellular matrix (ECM) in wound healing: a review, Biomimetics 7 (2022) 14–16, https://doi.org/10.3390/biomimetics7030087.
[68] G.S. Schultz, G.A. Chin, L. Moldawer, R.F. Diegelmann, Principles of wound healing, Diabet. Foot Probl. (2011) 395–402, https://doi.org/10.1142/9789812791535_0028.
[69] D. Markeson, J.M. Pleat, J.R. Sharpe, A.L. Harris, A.M. Seifalian, S.M. Watt, Scarring, stem cells, scaffolds and skin repair, J. Tissue Eng. Regen. Med. 9 (2015) 649–668, https://doi.org/10.1002/TERM.1841.